Propagating versus Nonpropagating Madden–Julian Oscillation Events

DAEHYUN KIM

Lamont-Doherty Earth Observatory, Columbia University, Palisades, New York

JONG-SEONG KUG

Korea Institute of Ocean Science and Technology, Ansan, South Korea

ADAM H. SOBEL

Lamont-Doherty Earth Observatory, Palisades, and Department of Applied Physics
and Applied Mathematics, Columbia University, New York, New York

(Manuscript received 3 February 2013, in final form 24 May 2013)

ABSTRACT

Basinwide convective anomalies over the Indian Ocean (IO) associated with the Madden–Julian oscillation (MJO) sometimes propagate eastward and reach the west Pacific (WP), but sometimes do not. Long-term observations and reanalysis products are used to investigate the difference between the propagating and nonpropagating MJO events. IO convection onset events associated with the MJO are grouped into three categories based on the strengths of the simultaneous dry anomalies over the eastern Maritime Continent and WP. The IO convection anomaly preferentially makes eastward propagation and reaches the WP when the dry anomaly is stronger.

Analysis of the column-integrated moist static energy (MSE) budget shows that horizontal advection moistens the atmosphere to the east of the positive MSE anomaly associated with the active convection over the IO and is of sufficient magnitude to explain the eastward propagation of the positive MSE anomaly. Interpretation is complicated, however, by lack of closure in the MSE budget. A residual term, of smaller but comparable magnitude to the horizontal advection, also moistens the column to the east of the positive MSE anomaly. Nonetheless, the authors decompose the horizontal advection term into contributions from different scales and find that a dominant contribution is from free-tropospheric meridional advection by the intraseasonal time scale wind anomalies. The positive meridional advection in between the convective and dry anomalies is induced by the anomalous poleward flow, which is interpreted as part of the Rossby wave response to the dry anomaly. The poleward flow advects the climatological MSE, which peaks at the equator, and moistens to the east of IO convective anomaly.

1. Introduction

The Madden–Julian oscillation (MJO) is the dominant mode of intraseasonal variability in the tropics (Madden and Julian 1972). A few distinct characteristics of the MJO are its vast horizontal scale (wavenumber 1–3), the time scale shorter than a season but longer than a month (30–60-day period), and the eastward propagation. The MJO interacts with many short-term weather and climate phenomena (Takayabu et al. 1999; Maloney and Hartmann 2000; Wheeler and McBride 2005; Kug et al. 2009), but understanding of the dynamics of its initiation, maintenance, and propagation is still elusive (Waliser 2005; Wang 2005; Zhang 2005).

Many MJO events initiate from or pass through the Indian Ocean (IO) (Matthews 2008). In a typical life cycle of the MJO (e.g., Wheeler and Hendon 2004), planetary-scale convective envelopes develop over the IO, propagate eastward, weaken over the Maritime Continent (MC) but still continue to propagate, and then reintensify upon reaching the west Pacific (WP). Not every MJO event, however, follows this typical ''life cycle'' of the MJO. Sometimes the anomalous convection over the IO ceases before it reaches the WP (Matthews 2008). This study is motivated by this observation, and focuses on the propagation of MJO convection from the IO to the WP. Our question is what makes the difference

---

Corresponding author address: Daehyun Kim, Lamont-Doherty Earth Observatory, Division of Ocean and Climate Physics, 61 Route 9W, Columbia University, Palisades, NY 10964-1000.
E-mail: dkim@ldeo.columbia.edu

DOI: 10.1175/JCLI-D-13-00084.1

between the propagating and nonpropagating MJO events? We address this question by analyzing observations and reanalysis data.

Historically, many MJO theories have regarded the MJO as a moist Kelvin wave (Lau and Peng 1987; Chang and Lim 1988; Emanuel 1987; Neelin et al. 1987; Wang 1988; Wang and Rui 1990). In these theories, the MJO shares its propagation mechanism with the equatorial Kelvin wave. A Kelvin wave does not require any diabatic heating for its existence. It propagates by gravity wave dynamics, that is, the linear interaction of buoyancy anomalies, pressure gradients, and the divergent flow in the presence of stable stratification. Interaction with deep convection modifies Kelvin wave dynamics but does not change the essence of the propagation mechanism. The phase speed of the eastward propagating waves in these theories, however, is close to that of the moist Kelvin wave ($15{\sim}20\,\mathrm{m\,s^{-1}}$), faster than that of the MJO ($\sim5\,\mathrm{m\,s^{-1}}$). Also, in wavenumber–frequency space, the MJO band is distinguished from that of the Kelvin wave (Wheeler and Kiladis 1999), although Roundy (2012) argued that the distinction between the MJO and the Kelvin wave is not clear. In these theories, horizontal variations of tropospheric moisture are often ignored. Moisture is treated as a diagnostic variable or as a fixed function of sea surface temperature.

More recently, a school of thought has emerged in which the MJO is regarded as what some investigators now call a "moisture mode" (Neelin and Yu 1994; Raymond 2000, 2001; Sobel et al. 2001; Sobel and Gildor 2003; Fuchs and Raymond 2002, 2005, 2007; Sugiyama 2009a,b; Majda and Stechmann 2009; Sobel and Maloney 2012, 2013; Sukhatme 2013). In these theories, moisture is prognostic. The horizontal or temporal variations of temperature, by contrast, may be ignored [the weak temperature gradient (WTG) approximation], and the anomalous convection associated with the MJO is often assumed to follow the anomalous column-integrated water vapor closely [although this need not be the case; e.g., Majda and Stechmann (2009) take water vapor and convection to be in quadrature]. Column-integrated moist static energy (MSE) or moist entropy may be used instead of water vapor as the explicit prognostic variable in these theories, both because these are the most nearly conserved variables in the system and because, consistent with the WTG, MSE or entropy variations are dominated by water vapor variations, with temperature variations being smaller. In these theories, the propagation of the MJO is caused by those processes that build up positive MSE tendencies to the east of the positive MSE anomaly.

There have also been attempts to explain the propagation mechanism of the MJO in comprehensive global model simulations in the context of moisture mode thinking. In an analysis of the MSE budget of the MJO simulated in an atmospheric general circulation model (GCM), Maloney (2009) found that horizontal advection of MSE was a term that best explained the eastward propagation, in that it dominated the positive tendency to the east of the positive MSE anomaly. Decomposition of the advection term into different scales of motion revealed in turn that the main contributor to the horizontal advection term was meridional advection by synoptic-scale eddies. The lower-tropospheric, planetary-scale easterly anomaly to the east of the positive MSE anomaly suppresses synoptic-scale activity. As this activity mixes dry subtropical air with moister equatorial air, reduction of this mixing by the planetary-scale easterlies causes moistening in an anomalous sense. Andersen and Kuang (2012), in their aquaplanet simulation with another atmospheric GCM, also found that modulation of synoptic-scale eddy activity by the MJO-scale wind variability plays an important role in the eastward propagation of the MSE anomaly.

Kiranmayi and Maloney (2011) analyzed the MSE budget of the MJO using reanalysis data. Their results are consistent with the modeling results of Maloney (2009) and Andersen and Kuang (2012) on both the role of horizontal advection generally and that associated with high-frequency eddy activity in particular.

In this study, we extend these studies by focusing even more closely on MJO propagation. We distinguish between MJO events in which MJO convection propagates from the IO to the WP and those in which it does not. We investigate what explains the propagation in the set of events in which propagation to the WP does occur, focusing on the column-integrated MSE budget. This is loosely motivated by studies of tropical cyclogenesis in which developing and nondeveloping disturbances are studied separately (e.g., McBride and Zehr 1981). As in previous studies, horizontal advection emerges as an important term, and we investigate the contributions to this term from different scales of motion.

In section 2, we describe the data and filtering methods used in this study. Propagation characteristics are distinguished according to the strength of the dry anomalies to the east of the IO convection, and the mechanism responsible for the difference between propagating and nonpropagating events is shown in section 3, followed by a summary and conclusions in section 4.

2. Data and method

We use daily-averaged outgoing longwave radiation (OLR) from the Advanced Very High Resolution Radiometer (AVHRR) (Liebmann and Smith 1996) as a proxy for deep convection in the tropics. Daily-averaged tropospheric winds, temperature, specific humidity, and

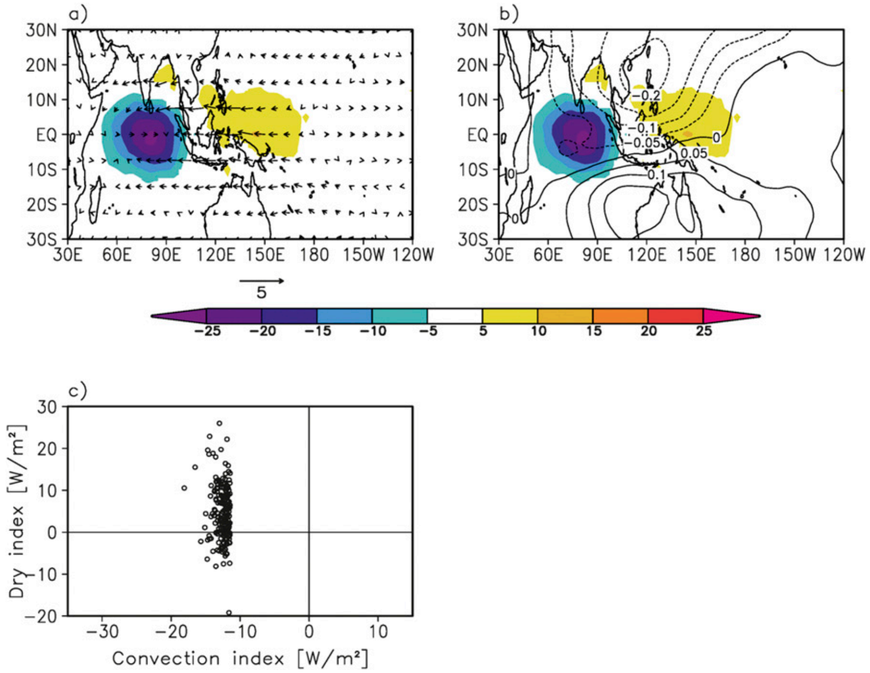

FIG. 1. Composited 850-hPa (a) wind (vectors, m s^{-1}) and (b) streamfunction (contours, $\times 10^{-7}$ m^2 s^{-1}) anomalies on top of OLR (shaded, W m^{-2}) anomalies for the events when the 15°S–15°N, 70°–100°E averaged, 20–100-day filtered OLR anomaly becomes lower than its negative standard deviation. OLR anomalies are shown only when they are statistically significant at 95% confidence level. (c) Scatterplot of convection (area averaged OLR anomaly over 15°S–15°N, 70°–100°E) and dry (over 15°S–15°N, 120°E–180°) indices.

geopotential height were taken from the Interim European Centre for Medium-Range Weather Forecasts Re-Analysis (ERA-Interim) (Dee et al. 2011). The surface latent and sensible heat fluxes and longwave and shortwave radiative fluxes at the surface and the top of the atmosphere are also obtained from ERA-Interim. OLR and ERA-Interim data during the period 1979–2009 were used. All variables were interpolated into a 2.5° latitude × 2.5° longitude grid before any calculations. A composite daily seasonal cycle was removed from all variables to produce daily anomalies and then the anomalies were bandpass filtered using a 201-point Lanczos filter (Duchon 1979) to retain only 20–100-day variability. The MJO-filtered anomaly was obtained by Fourier and inverse-Fourier transform, retaining only eastward propagating wavenumbers 1–9 and 30–96-day periods (Wheeler and Kiladis 1999).

3. Results

a. Propagation characteristics

The 20–100-day bandpass-filtered OLR anomaly is averaged over 15°S–15°N, 70°–100°E to obtain an eastern IO convection index (CI). Then, we seek days when the CI becomes lower than one negative standard deviation and use as a reference date for each event the first day of any multiple-day period when this threshold is met. We choose one standard deviation as a threshold value to ensure that both the amplitude of the CI and the number of selected events are large enough. Note that the results below are not sensitive to the threshold value. There are 189 such cases during the period of interest (1979–2009). The 20–100-day filtered OLR and 850-hPa wind anomalies are composited for those days and shown in Fig. 1a.

In Fig. 1a, the center of the anomalous convection is located over the central Indian Ocean. Positive OLR anomalies, indicating suppressed convection and dry conditions, are located farther to the east. An easterly low-level wind anomaly resides between the negative and positive OLR anomalies. The easterly anomaly might be a combination of a Kelvin wave response to the enhanced convection over the IO and a Rossby wave response to the suppressed convection over the MC and WP. Weak poleward meridional wind anomalies can be also found in both hemispheres (e.g., 10°N, 120°E). The rotational component of the flow pattern can be visualized with the 850-hPa streamfunction anomaly (Fig. 1b). In between the IO and the WP the streamfunction anomaly exhibits a dipole structure straddling the equator. We interpret this as a Rossby wave signature forced by the anomalous reduction of convective heating associated with the dry anomaly

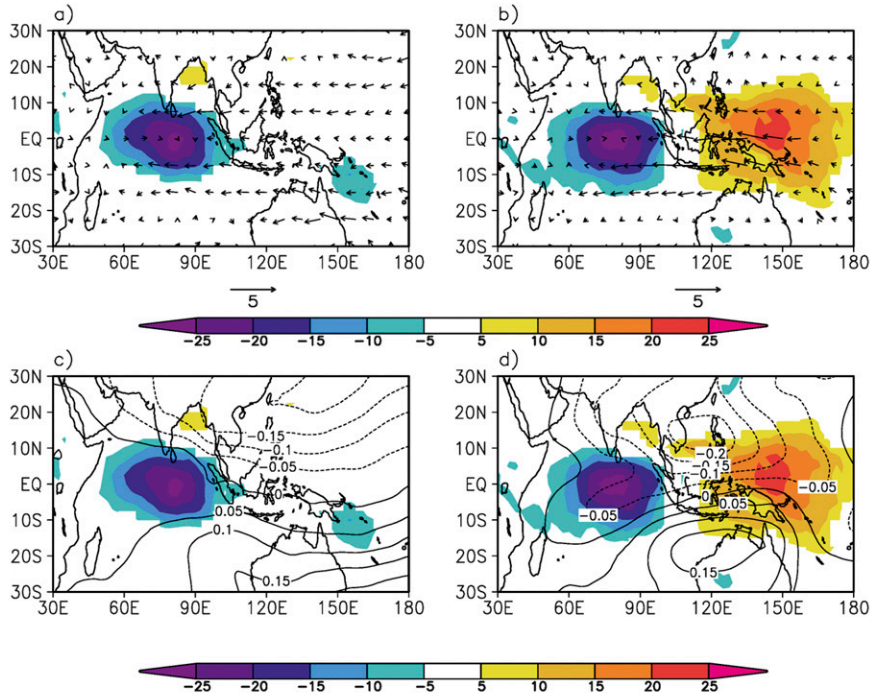

FIG. 2. As in Figs. 1a and 1b, but for (a),(c) weak and (b),(d) strong dry cases.

since long Rossby waves have westward group velocity. Anomalous poleward flow also occurs farther west, at the longitudes of the positive anomaly in convective heating in the IO, and may be partly attributable to the "Sverdrup" component, which we would expect in a steady state (with meridional advection of planetary vorticity balancing vortex stretching associated with the heating; Gill 1980). In the following sections we will focus on the role of the dry anomaly over the MC and the WP in the eastward propagation of the enhanced convection.

To investigate the role of the dry anomaly, a dry index (DI) is defined as the area averaged OLR anomaly over 15°S–15°N, 120°E–180°. Figure 1c is a scatterplot of the CI versus the DI for all 189 cases. Because we searched for days when the CI first becomes less than one standard deviation ($-11.46\,\mathrm{W\,m^{-2}}$) below the mean, the composite CI on those days is close to that value. In Fig. 1c, the DI exhibits a significant scatter from around $-10\,\mathrm{W\,m^{-2}}$ to higher than $20\,\mathrm{W\,m^{-2}}$, indicating that the dryness to the east of the convection anomaly over the eastern IO is not tightly coupled to the convection anomaly itself.

Using the 189 DI values, we calculated the mean and the standard deviation of the DI and then grouped the events into three categories according to their DI values. When the DI is greater than its mean plus half of its standard deviation, the event is classified as a strong dry case, whereas when DI is less than its mean minus half its standard deviation it is classified as a weak dry case. Results are similar if we use one standard deviation of the DI in classifying the events instead of one-half standard deviation. Given the insensitivity of the results to the threshold value, we present results computed using a half standard deviation in order to increase our sample size. The remaining events are classified as moderate dry cases. As a result, 78 strong and 71 weak dry events are identified. Next we focus on the contrast between strong and weak dry events in terms of the different propagation characteristics of their convection anomalies over the IO.

Composite maps of OLR and 850-hPa wind and streamfunction anomalies for the weak and strong dry cases separately are presented in Fig. 2. Although the negative OLR anomalies over the IO in the strong dry composite have slightly broader spatial extent, the peak values are similar in both cases. This implies that the difference in the dry anomalies over the MC and the WP is not due to differences in the strength of the IO convection anomaly. By construction, there is a notable difference in the magnitudes of the dry anomalies over the MC and the WP region. The easterly and poleward meridional wind anomalies associated with the streamfunction anomalies straddling the equator to the east of the enhanced convection are also stronger in the strong dry cases than that for the weak dry case. This supports our previous interpretation of these wind and streamfunction anomalies as a Rossby wave response to the reduction in convective heating associated with the dry anomaly.

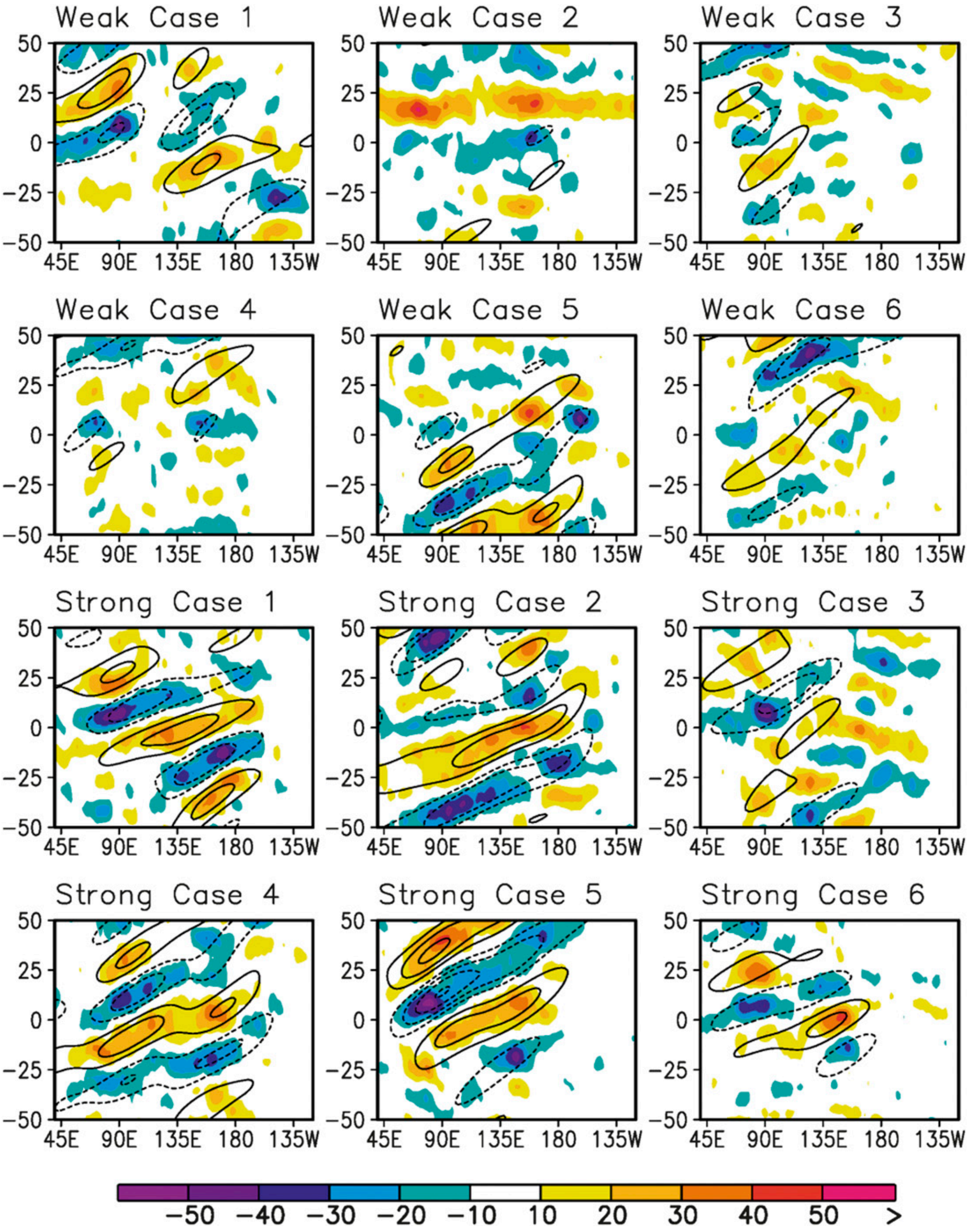

FIG. 3. Hovmöller diagram of 15°S–15°N averaged, 20–100-day filtered (shaded) and MJO filtered (contours) OLR ($\mathrm{W\,m^{-2}}$): contour interval 10 $\mathrm{W\,m^{-2}}$, zero line not displayed. The six weakest and six strongest dry cases are presented.

Figure 3 presents Hovmöller diagrams of 15°S–15°N averaged, 20–100-day filtered (shaded) and MJO-filtered (contour) OLR anomalies for the six weakest and strongest dry events. Although this is a limited number of samples, these cases are representative of others in their categories. Day 0 in each case represents the day when the CI first becomes less than one standard deviation below its mean. When the dry anomaly to the east is weak (upper six panels in Fig. 3), the OLR anomaly over the IO tends to stop propagating before it reaches the WP in many events (e.g., weak dry cases 1, 3, 5, and 6). On the other hand, when the dry anomaly is strong (lower six panels in Fig. 3), the convection anomaly over the IO propagates through the MC and reaches the WP in most of the events.

TABLE 1. MJO characteristics according to the dry index.

Characteristic	Weak dry	Strong dry
Number of MJO events	41 (71)	44 (78)
MJO zonal extent (°)	33.2	60.2
MJO duration (days)	18.8	26.3

The zonal extent and duration of the MJO events are defined using the 15°S–15°N averaged MJO-filtered OLR anomalies. From the IO convection onset days identified above, we track the movement of the minimum OLR value over time until it becomes greater than $-10\,\mathrm{W\,m^{-2}}$. The zonal extent of the MJO propagation is defined as the difference between the longitude of minimum OLR on the last day of tracking and that on day 0. The duration of the MJO is the period from day 0 to the last day. We exclude any event in which the minimum MJO-filtered OLR anomaly is higher than $-10\,\mathrm{W\,m^{-2}}$ on day 0 (e.g., weak case 6 in Fig. 3a). After this filtering, 41 and 44 events remain in the weak and strong dry categories, respectively. Our results and conclusions are not sensitive to the inclusion of those events.

Table 1 summarizes these characteristics of the weak and strong dry MJO events. The average MJO zonal extent for the weak dry cases (33.2°) is only about 55% of that of the strong dry cases (60.2°). Because the center of convection on day 0 is around 70°–100°E, the mean zonal extent of 33.2° means that the convection anomaly usually stops propagating before it reaches the WP. Consistent with the zonal extent, the duration of the MJO convection anomaly is also about 39% longer in the strong dry cases (26.3 days) compared with that in the weak dry cases (18.8 days). The differences in the MJO zonal extent and duration are statistically significant at the 95% confidence level in a one-tailed Student's t test. These statistics show that a convection anomaly over the IO that accompanies a stronger dry anomaly in the eastern MC and the WP lives longer and propagates farther eastward than one that accompanies a relatively weaker dry anomaly. This suggests an important role for WP dryness in the propagation of the MJO from the IO to the WP.S

b. Column-integrated moist static energy budget

To understand the dynamics behind the difference in the propagation characteristics of the weak and strong dry events, we analyze the column-integrated MSE budget in this section. The MSE (m) is the sum of sensible, latent heat, and potential energy of an air parcel:

$$m = C_p T + gz + L_v q, \qquad (1)$$

where T is temperature, z is geopotential height, q is specific humidity, C_p is the specific heat of air at constant pressure, g is the gravitational acceleration, and L_v is the latent heat of vaporization. The column-integrated MSE budget consists of 1) horizontal and 2) vertical advection, 3) surface turbulent latent and sensible heat fluxes, and 4) shortwave and longwave radiative heating:

$$\frac{\partial\langle m\rangle}{\partial t} = -\langle \mathbf{v}\cdot\nabla m\rangle - \left\langle w\frac{\partial m}{\partial p}\right\rangle + \mathrm{SH} + \mathrm{LH} + \langle \mathrm{SW}\rangle + \langle \mathrm{LW}\rangle, \qquad (2)$$

where angle brackets represent mass-weighted vertical integration from 1000 to 100 hPa, $\mathbf{v}$ is the horizontal wind vector, w is pressure velocity, p is pressure, SH (LH) is the surface sensible (latent) heat flux, and SW (LW) is the shortwave (longwave) radiative heating rate. As will be shown below, our column-integrated MSE budget is not closed; a nonnegligible residual, which is the lhs of Eq. (2) minus sum of all terms in rhs of Eq. (2), is found. The residual term might originate from the analysis increment in the assimilation system of ERA-Interim, which means that there are missing moistening/drying processes associated with the MJO. Calculating advection terms on a grid configuration that is different from the native model grid (as we have to do, lacking the data on the original model levels) might also contribute to the residual. Kiranmayi and Maloney (2011) also reported the existence of a large residual from ERA-Interim in the MSE budget associated with the MJO. Mapes and Bacmeister (2012) find a qualitatively similar result in the National Aeronautics and Space Administration Modern-Era Retrospective Analysis for Research and Applications (MERRA) reanalysis. They show that the analysis increment in the moisture budget, an indication of missing physics in the model, is significant and positive in the Pacific ahead of active MJO phases moving eastward from the Indian Ocean.

In Fig. 4, composited Hovmöller diagrams of 10°S–10°N averaged OLR (contour) and MSE (shaded; hereafter MSE refers to the column-integrated MSE unless otherwise explained) anomalies for the weak and strong dry cases are presented. As shown above in Table 1, the weak dry cases exhibit limited propagation of the negative OLR anomaly, ceasing around 120°E and day 10, while in the strong dry cases the OLR anomaly propagates to around 180°. The composite may not represent all individual events perfectly as the OLR anomalies in individual events propagate with different phase speeds. Still, the composite captures the overall difference in MJO propagation between the two categories. The MSE anomaly is consistent with the OLR anomaly. The strong

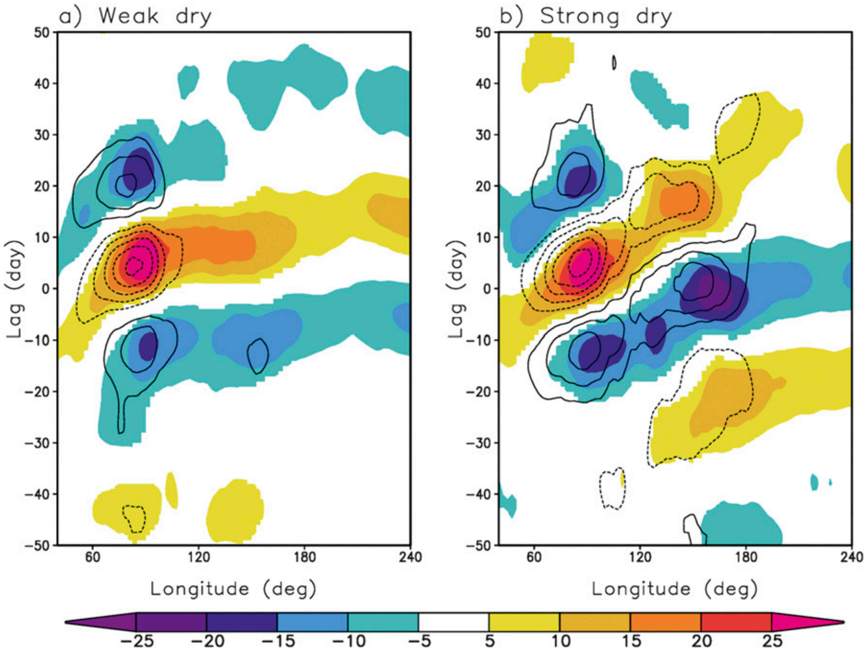

FIG. 4. Composited Hovmöller diagram of OLR ($\mathrm{W\,m^{-2}}$, contours), and vertically integrated MSE anomaly ($\mathrm{J\,m^{-2}}$ scaled by an arbitrary number 3×10^5, shaded) anomaly for (a) weak and (b) strong dry cases. MSE anomalies are shown only when they are statistically significant at 95% confidence level. Solid (dashed) lines represent positive (negative) values; contour interval is $5\,\mathrm{W\,m^{-2}}$, zero line not plotted.

dry case shows eastward propagation on the MJO time scale, which is absent in the weak dry case. This suggests that understanding what causes the eastward propagation of the MSE anomaly would be helpful to understand the cause of the propagation of the OLR anomaly.

Figure 5 exhibits the anomalous MSE budget terms together with the MSE anomaly itself for the strong dry case. The horizontal and vertical advection, the longwave radiative heating, the sum of surface turbulent sensible and latent heat flux and shortwave radiative heating, the residual, and the tendency [lhs of Eq. (2)] terms are displayed in separate panels in Fig. 5, with the MSE anomaly superimposed on each. In Fig. 6, all terms considered and the MSE anomaly are averaged between lag −5 and +5 and shown in line plots as functions of longitude for easier comparison.

Figures 5 and 6 show that the horizontal advection term has a dominant positive contribution around 100°–140°E in between negative and positive MSE anomalies, suggesting an important role for horizontal advection in the propagation of the MSE anomaly. Although the longwave and vertical advection terms have larger amplitudes, they are out of phase and therefore cancel each other (Fig. 6). Both are also closer to in phase (in the case of longwave) or out of phase (in the case of vertical advection) with the MSE itself, while horizontal advection is more nearly in quadrature, being the largest term at the location of the MSE zero crossing, around 120°E. The positive anomaly of the sum of surface turbulent fluxes and shortwave is partly in phase with the positive MSE anomaly, suggesting its role in destabilizing the MSE anomaly, but it lags the MSE anomaly and therefore cannot explain the eastward propagation. These results demonstrate 1) the destabilizing effect of the longwave radiative heating and latent heat flux, 2) the stabilizing effect of the vertical advection term, and 3) the importance of the horizontal advection term to propagation of the MSE anomaly.

Figure 7 shows differences between the budget terms and MSE anomalies found in the strong dry cases and those in the weak dry cases. The difference in the horizontal advection term is the largest of the differences in the terms that moisten the atmosphere between the IO and WP (around 120°E, Fig. 7a). This shows that horizontal advection moistens the atmosphere to the east of the IO convection more strongly in the strong dry cases than in the weak dry cases. The differences in vertical advection also show positive value near 120°E but, as mentioned earlier, this term is mostly canceled by the longwave term (Fig. 7b).

The overall magnitude of the large residual that leads the positive MSE in Figs. 5 and 6 is comparable to those

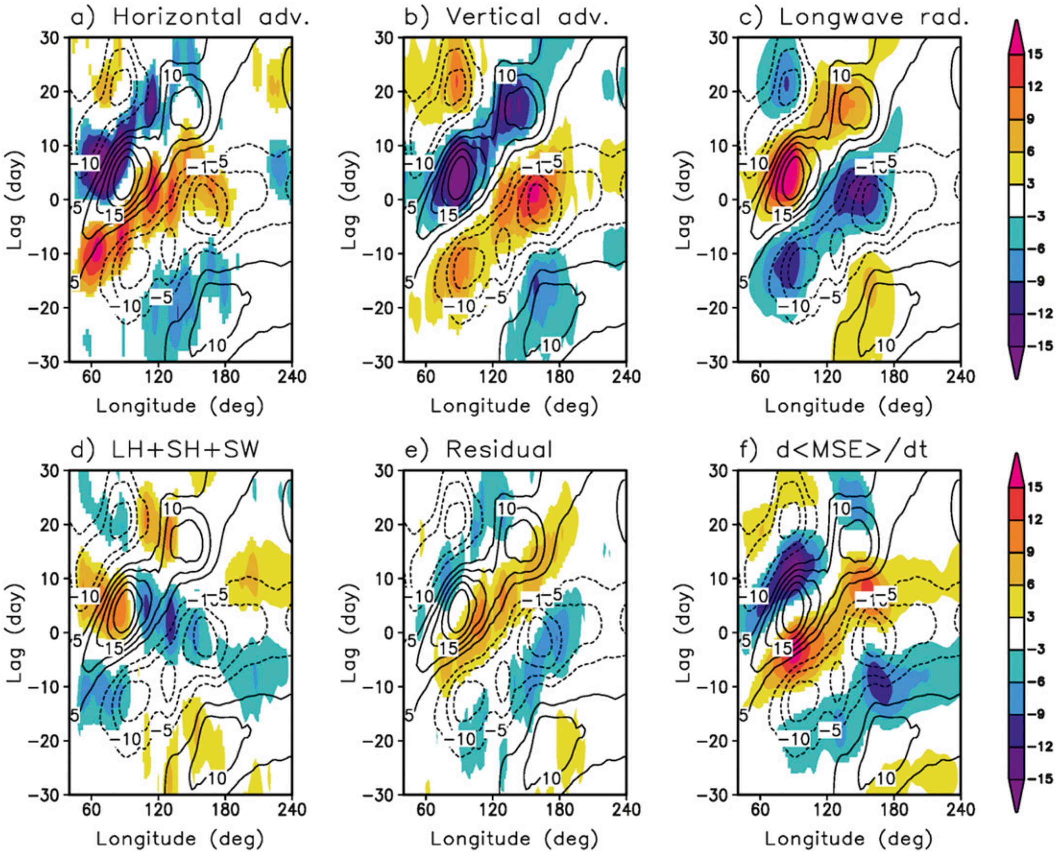

FIG. 5. Composited Hovmöller diagram of anomalous (a) horizontal and (b) vertical advection term of the column-integrated MSE budget, (c) sum of longwave radiative fluxes at surface and the top of the atmosphere, (d) sum of surface latent and sensible heat flux and shortwave radiative fluxes at surface and the top of the atmosphere, (e) residual term, and (f) tendency term for strong dry events. MSE budget terms are shown only when they are statistically significant at 95% confidence level. Contoured in each panel is column-integrated MSE (J m^{-2} scaled by an arbitrary number 3×10^5) anomaly; contour interval is 5 in scaled value.

of other budget terms, although it is overall smaller than that of the horizontal advection term, especially where the MSE anomaly is close to zero (Fig. 6). This suggests that there is either a missing moistening processes associated with the MJO in the ERA-Interim data or a numerical error in the calculation of advection terms, perhaps resulting from the use of constant pressure level data rather than data on the original model grid. We also find a significant residual to the east of the enhanced convection in the weak dry case. In Fig. 7a, the difference of the residual term between the strong and weak dry cases are small near 120°E, showing that a residual term with similar amplitude exists also in the weak dry cases. The similarity of the strong and weak dry cases in this regard suggests, at least, that the residual is not crucial to the difference between the two types of cases and, thus, does not contain the fundamental explanation for the propagation of the MJO. The existence of the large residual imposes a caveat on our interpretation, but does not deter us from treating the advection term as significant and analyzing it further.

To diagnose the process responsible for the anomalous horizontal advection in the region between the IO convection and the WP dry anomaly, the horizontal advection term is decomposed into zonal and meridional advection terms in Fig. 8. The zonal and meridional advection are time averaged from lag −5 to +5 and shown as line plots in Fig. 9, together with the MSE anomaly similarly averaged. Meridional advection dominates over the west Pacific and Maritime Continent. Zonal advection plays a relatively greater role over the eastern IO and MC, being comparable to (although for the most part still smaller than) the meridional advection there, before becoming smaller in the MC. The relatively larger role of the zonal advection over the IO is consistent with the results of Hsu and Li (2012) and suggests its possible importance in the initiation of the MJO. The meridional advection term is further decomposed into contributions

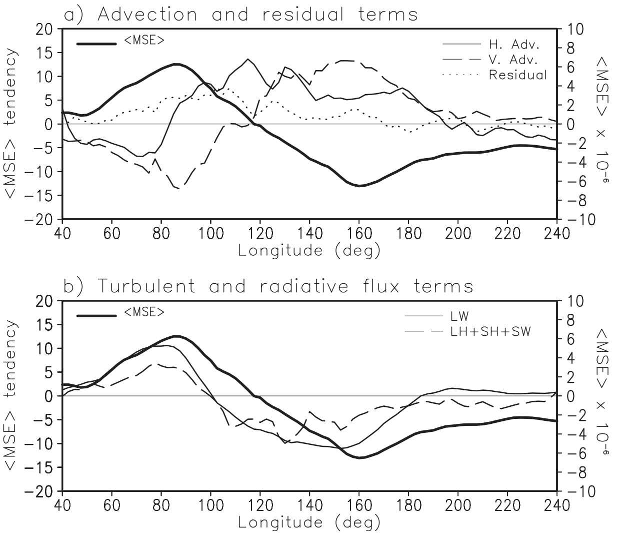

FIG. 6. Column-integrated MSE budget terms for strong dry events: (a) horizontal advection (W m^{-2}, black solid), vertical advection (W m^{-2}, black dashed), and residual (W m^{-2}, black dotted) and (b) longwave radiative fluxes (W m^{-2}, black solid) and sum of surface latent and sensible heat flux and shortwave radiative fluxes at the surface and the top of the atmosphere (W m^{-2}, black dashed). Anomalous column-integrated MSE ($\times 10^{-6}$ J m^{-2}, blue) is plotted in both panels as a reference. All quantities are averaged over lag day −5 to +5.

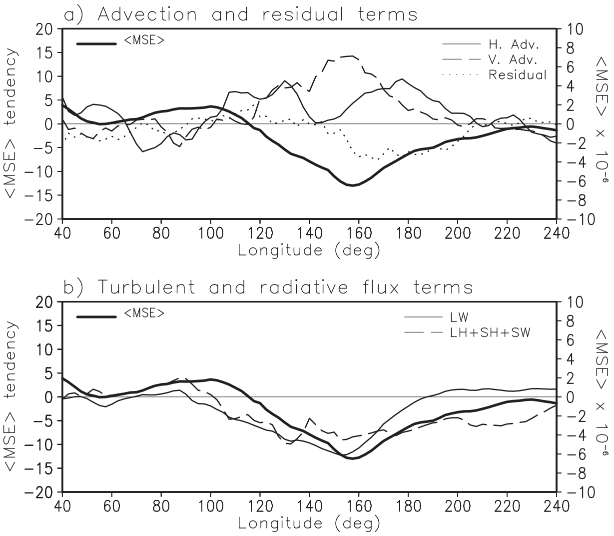

FIG. 7. As in Fig. 6, but for differences between column-integrated MSE budget terms for strong and weak dry events.

from the PBL (defined as the layer from 1000 to 850 hPa) and from the free troposphere (Fig. 10). The contribution from PBL is minor, and the free-tropospheric meridional advection dominates.

The free-tropospheric meridional advection term can be expressed in equation form as

$$-\left\langle\left\langle v\frac{\partial m}{\partial y}\right\rangle\right\rangle', \tag{3}$$

where double angle brackets represent the mass-weighted vertical integration from 850 to 100 hPa and the prime (′) represents the 20–100-day filtered anomaly. We further decompose this term as

$$-\left\langle\left\langle v\frac{\partial m}{\partial y}\right\rangle\right\rangle' \approx -\left\langle\left\langle \overline{v}\frac{\partial m'}{\partial y}\right\rangle\right\rangle' - \left\langle\left\langle v'\frac{\partial \overline{m}}{\partial y}\right\rangle\right\rangle' - \left\langle\left\langle v''\frac{\partial m''}{\partial y}\right\rangle\right\rangle', \tag{4}$$

where the overbar represents the climatological seasonal cycle, and double primes the 20-day high-pass filtered anomaly. Of these, the second term in Eq. (4) dominates the others. In Fig. 11, the column-integrated MSE anomaly, the total tropospheric meridional advection [lhs in Eq. (4)], and the second term in rhs of Eq. (4), all averaged from day −5 to +5, are displayed. This figure demonstrates that 1) the free-tropospheric meridional advection term moistens the atmosphere in front of the positive MSE anomaly and 2) the advection of climatological MSE by the anomalous meridional wind explains most of that advective moistening.

It is of interest what fraction of the free-tropospheric meridional advection comes from higher-frequency, synoptic-scale eddies because recent modeling and observational studies show that a significant contribution comes from it (Maloney 2009; Kiranmayi and Maloney 2011; Anderson and Kuang 2012). We refer here to the high-frequency eddy fluctuations with period shorter than 20 days, represented by the third term in Eq. (4). This term is plotted, together with the MSE anomaly and total meridional advection, in Fig. 12. The figure shows that the contribution from the high-frequency eddies is not negligible but is not the dominant factor either. The high-frequency eddies explain a larger fraction of the tropospheric meridional advection in the later phases of the propagation but still are not a major factor then (not shown). Therefore, the importance of the high-frequency eddies in the propagation of MJO convection in our results is smaller than in previous studies. We hypothesize here that this is because we focus on the moistening processes over the MC, where free-tropospheric meridional advection by the high-frequency eddies has smaller variance than that over the IO and the WP (Fig. 13a). The ratio of high-frequency eddy meridional advection to the variance of total free-tropospheric meridional advection also has a minimum over the MC (Fig. 13b). In previous studies, analysis of the MSE budget

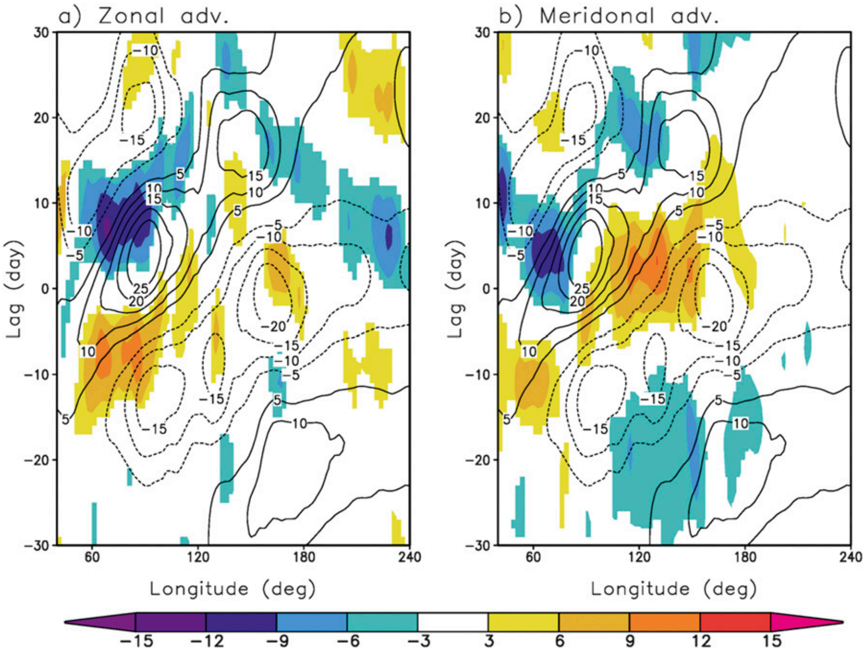

FIG. 8. Composited Hovmöller diagram of anomalous (a) zonal and (b) meridional advection term of the column-integrated MSE budget for strong dry events. MSE budget terms are shown only when they are statistically significant at 95% confidence level. Contoured in each panel is column-integrated MSE (J m^{-2} scaled by an arbitrary number 3 × 10^{5}) anomaly; contour interval is 5 in scaled value.

was done using simulations of an ocean-covered planet in GCMs (Maloney 2009; Anderson and Kuang 2012), or analysis was done over the oceanic areas to the east and west of the MC (but not in the MC itself) in reanalysis data (Kiranmayi and Maloney 2011).

Figure 14 shows how the meridional advection moistens the atmosphere in between the convection and dry anomalies. In Fig. 14, the 750-hPa meridional wind anomaly (shaded) is poleward from the equator in both hemispheres over the longitudes between the convection and dry anomalies (Fig. 2b). At the same time, the time-mean MSE (contour) shows a structure that peaks at the equator. Therefore the poleward meridional wind anomalies flow from higher to lower MSE, thereby inducing anomalous moistening in a meridional average over any plausible width (e.g., 5°S–5°N or 10°S–10°N) centered on the equator.

The above results show that enhanced free-tropospheric meridional advection of the MSE leads to the propagation of the MSE anomaly in the strong dry cases and that the interaction of the meridional anomaly with climatological MSE induces the meridional advection. What then is the cause of the poleward meridional wind anomaly? We expect the wind response to the anomalous heating associated with the enhanced convection anomaly to be similar in both weak dry and strong dry cases, barring significant differences in the vertical structure of the heating, because the positive convective anomalies in both have similar strength (Fig. 2). On the other hand, we expect the responses to the WP heating anomalies to be quite different as the total diabatic heating is presumably quite different. Investigation of upper and

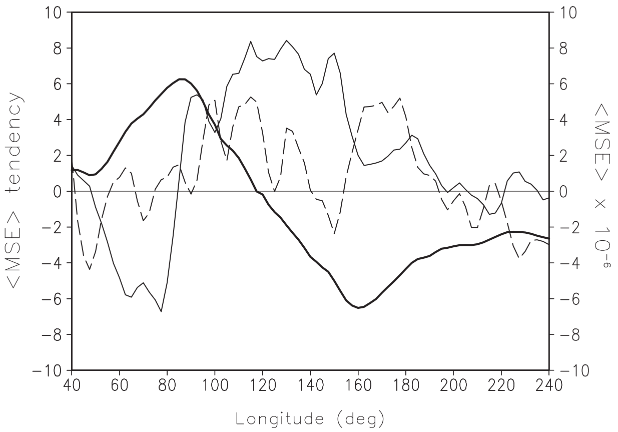

FIG. 9. Anomalous -ntegrated MSE (×10^{-6} J m^{-2}, blue) and column-integrated MSE budget terms of the zonal advection (W m^{-2}, black dashed), and meridional advection (W m^{-2}, black solid) for strong dry events: all quantities averaged over lag day −5 to +5.

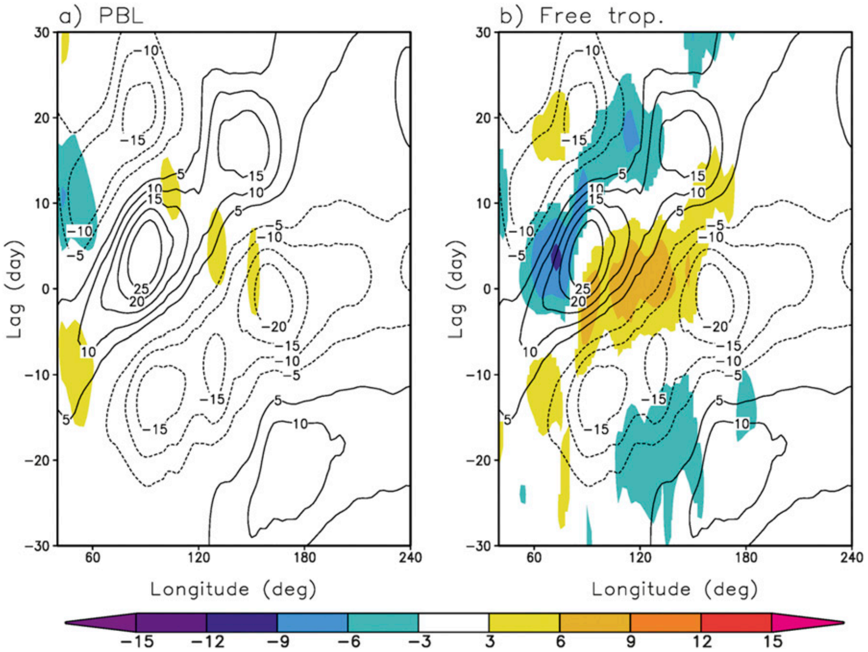

FIG. 10. Composited Hovmöller diagram of contribution from the (a) PBL and (b) free troposphere to the anomalous meridional advection term of the column-integrated MSE budget for strong dry events. MSE budget terms are shown only when they are statistically significant at 95% confidence level. Contoured in each panel is column-integrated MSE ($\mathrm{J\,m^{-2}}$ scaled by an arbitrary number 3×10^5) anomaly; contour interval is 5 in scaled value.

lower tropospheric circulation anomalies (not shown) suggests that the enhanced poleward wind anomalies over the MC are Rossby wave responses to the negative heating anomaly to the east (Matsuno 1966; Gill 1980). This again suggests that the dry anomaly over the eastern MC and WP plays a dynamically active role in the propagation of IO convection, through the wave response to the reduced heating there and the meridional moisture advection to the west driven by this response.

4. Conclusions

We have investigated the propagation of MJO convective anomalies from the Indian Ocean to the west Pacific, using observed OLR, surface latent heat and longwave fluxes, and reanalysis wind fields. When enhanced convection is located over the IO, there is a dry anomaly over the eastern Maritime Continent and the WP. The strength of the dry anomaly is not strongly related to the strength of the convective anomaly over the IO. The propagation of the MJO convection from the IO to the WP, however, is strongly related to the strength of the dry anomaly (associated with the positive OLR anomaly) over the eastern MC and the WP. When the dry anomaly is strong, the MJO convection over the IO tends to propagate to the WP. When the dry anomaly is weak, the propagation usually ceases before the convection reaches the WP.

The column-integrated MSE budget is examined to understand the difference in propagation characteristics between the weak and strong dry cases. Our results show that the horizontal advection term plays an important

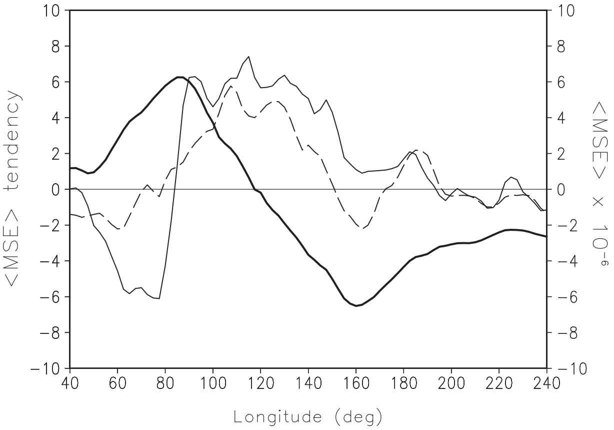

FIG. 11. Anomalous column-integrated MSE ($\times 10^{-6}\,\mathrm{J\,m^{-2}}$, blue), free-tropospheric meridional advection ($\mathrm{W\,m^{-2}}$, black solid), and meridional advection by interaction between seasonal cycle of MSE and 20–100-day filtered meridional wind anomaly ($\mathrm{W\,m^{-2}}$, black dashed) for strong dry events: all quantities averaged over lag day −5 to +5.

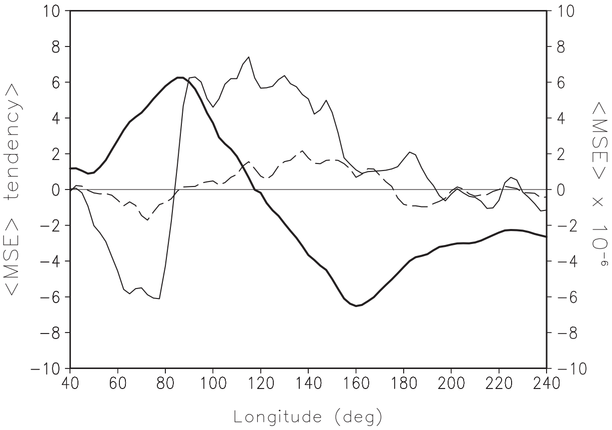

FIG. 12. As in Fig. 11, but for the meridional advection by high-frequency disturbances (W m^{-2}, black, dashed) for strong dry events.

role in the propagation of the IO convection, in that it has its greatest value and exceeds other terms, in the MC region, between the moist static energy (MSE) maximum in the IO and the minimum in the WP. The radiative terms, especially the longwave component, and the surface turbulent heat flux terms maximize closer to the MSE maximum (with the latent heat flux lagging it somewhat) so that they act to amplify the MSE maximum but do not aid propagation. A significant residual term, which contributes to the moistening to the east of convection with a smaller but comparable magnitude with that of the horizontal advection, complicates interpretation of our budget analysis. This is qualitatively consistent with the results of Kiranmayi and Maloney (2011) and Mapes and Bacmeister (2012). While it is possible that numerical limitations of our computations are part of the reason for the residual, the consistency and systematic nature of the residuals in these different studies suggests that the current generation of reanalysis products may not yet be fully adequate for a fully satisfactory analysis of the moist static energy budget of the MJO. Nonetheless, the terms that are resolved tell a clear enough story that we proceed to analyze them further.

The decomposition of the horizontal advection term into zonal and meridional advection shows that the meridional advection term is most important for the propagation. The zonal advection term contributes more over the IO, suggesting its potential role in MJO initiation. Further decomposition of the meridional advection term showed that contributions from the PBL are minor compared to those from the free troposphere. It is also found that the intraseasonal meridional wind anomalies are more important to the advection than those associated with the high-frequency eddies over the MC region. In strong dry cases, the free-tropospheric meridional advection moistens the atmosphere to the east of IO convection, providing a favorable condition for IO convection to move eastward.

These results suggest that the dry anomaly over the eastern MC and the WP plays a dynamically active role in the propagation of the IO convection through the

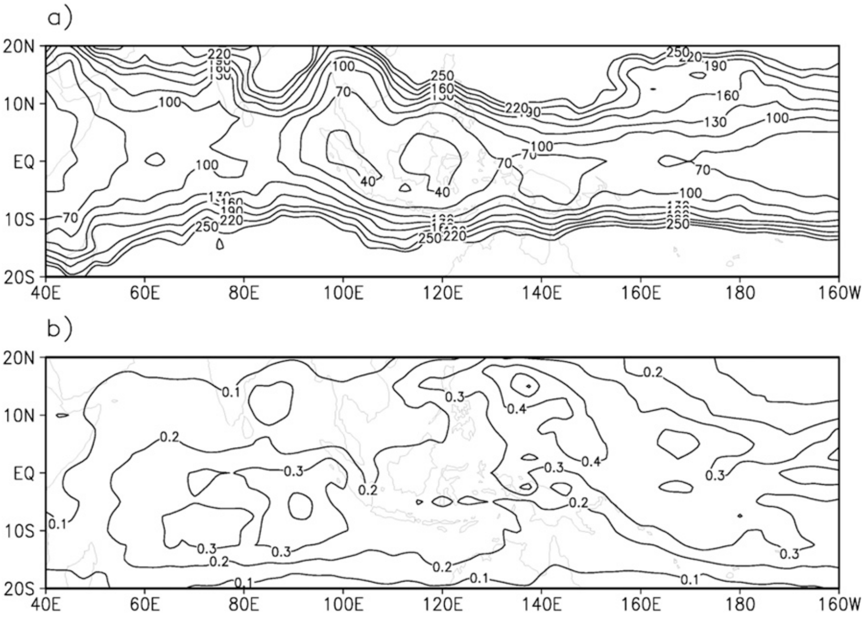

FIG. 13. (a) Variance of the free-tropospheric meridional advection by high-frequency eddies (W^2 m^{-4}) and (b) its fraction to the variance of total free-tropospheric meridional advection (unitless). Contour begins at 40 with interval 30 in (a), while it begins at 0.1 with interval 0.1 in (b).

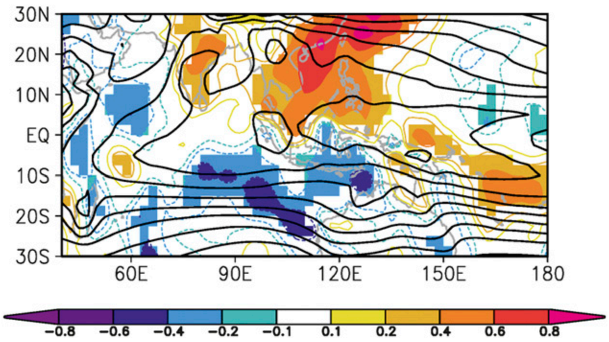

FIG. 14. Anomalous meridional wind (m s^{-1}, shaded and colored contours), averaged between lag day -5 to $+5$ for the strong dry cases, and time-mean MSE (kJ m^{-2}, black contours). Meridional wind anomalies are shaded when they are statistically significant at 95% confidence level. Both variables are those at 750 hPa.

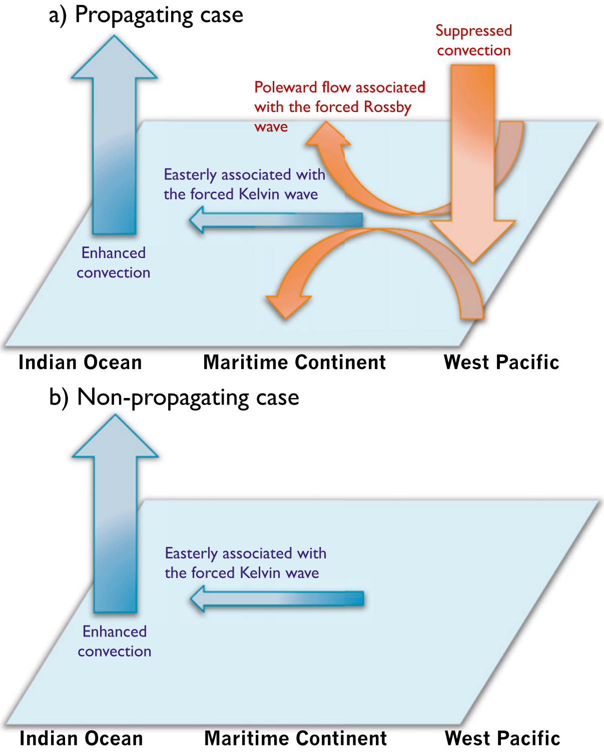

FIG. 15. Schematic representation of the key difference between the propagating and nonpropagating events.

Rossby wave response to it. The strong negative anomaly in convective heating presumably drives a planetary-scale Rossby wave response that includes the poleward flow anomalies we find to the west of the dry anomaly in both hemispheres. These poleward wind anomalies, together with the mean MSE pattern, which peaks at the equator, combine to form positive anomalous meridional advection to the east of the IO convection. This advective moistening appears, in our analysis, to be the primary factor that drives the positive MSE anomaly in the IO, and presumably the convection associated with it, to propagate eastward.

Figure 15 schematically shows the difference between the propagating and nonpropagating MJO events. In both events, enhanced convection with similar strength is located in the IO with the forced Kelvin wave response to the east of the convective anomaly. Because the magnitudes of the positive heating anomalies in the active convective regions are similar, the Kelvin wave responses over the MC should be similar. In this circumstance, any theory in which the Kelvin wave component is crucial for the propagation cannot explain the difference between the two types of events.

In the propagating MJO events, contrary to the nonpropagating events, convective activity over the eastern MC and the WP is anomalously suppressed. This additional negative heating anomaly excites a Rossby wave response to the west, which includes a lower-tropospheric poleward wind anomaly in between the enhanced and suppressed convective anomalies. The poleward meridional winds in both hemispheres advect moist air near the equator poleward, which moistens the lower troposphere. The moistening provides a favorable condition for the IO convection to propagate eastward.

Our finding suggests that the dry anomaly over the WP can be used in statistical MJO forecasts as a precursor of the MJO propagation when MJO convection is located over the IO. Regarding the important role of the dry anomaly ahead of the MJO convection over the IO, it is of practical importance whether contemporary state-of-the-art climate and weather prediction models properly simulate the dry anomaly. This is because it is still a tough test for a climate model to simulate the MJO adequately (Lin et al. 2006; Kim et al. 2009). Our preliminary analysis suggests that models with better MJO simulations also simulate relatively stronger dry anomalies to the east of the IO MJO convection. This relationship will be investigated in future work.

The important role played by meridional advection of moist static energy here is in contrast to most MJO theory. The great majority of simple models for the MJO do not include this process at all. Meridional advection was crucial to propagation in the simple moisture modes of Sobel et al. (2001), causing eastward propagation for an equatorward moisture gradient, as found here; but this theory was not quite appropriate to the MJO because it was formulated on an *f* plane rather than a meridional beta plane. Sukhatme (2013) extends the analysis of Sobel et al. (2001) to the equatorial beta plane and finds the same qualitative effect of meridional moisture gradients on propagation. The highly idealized model of Sobel and Maloney (2012, 2013) does include explicit

MSE advection, but only by the zonal flow. Sobel and Maloney considered a crude parameterization of meridional advection by synoptic-scale eddies. Our results suggest that meridional moisture advection by the planetary-scale flow should be included in MJO models of all levels of complexity, especially when they model MJO propagation through the Maritime Continent.

Acknowledgments. This work was supported by the NASA Modeling and Analysis program through Grant NNX09AK34G and by a grant from the National Research Foundation of Korea funded by the South Korean Ministry of Education, Science, and Technology (MEST) (NRF-2009-C1AAA001-2009-0093).

REFERENCES

Andersen, J. A., and Z. Kuang, 2012: Moist static energy budget of MJO-like disturbances in the atmosphere of a zonally symmetric aquaplanet. *J. Climate,* **25,** 2782–2804.

Chang, C.-P., and H. Lim, 1988: Kelvin wave-CISK: A possible mechanism for the 30–50 day oscillations. *J. Atmos. Sci.,* **45,** 1709–1720.

Dee, D. P., and Coauthors, 2011: The ERA-Interim reanalysis: Configuration and performance of the data assimilation system. *Quart. J. Roy. Meteor. Soc.,* **137,** 553–597.

Duchon, C. E., 1979: Lanczos filtering in one and two dimensions. *J. Appl. Meteor.,* **18,** 1016–1022.

Emanuel, K. A., 1987: An air–sea interaction model of intraseasonal oscillations in the tropics. *J. Atmos. Sci.,* **44,** 2324–2340.

Fuchs, Z., and D. J. Raymond, 2002: Large-scale modes of a nonrotating atmosphere with water vapor and cloud–radiation feedbacks. *J. Atmos. Sci.,* **59,** 1669–1679.

——, and ——, 2005: Large-scale modes in a rotating atmosphere with radiative–convective instability and WISHE. *J. Atmos. Sci.,* **62,** 4084–4094.

——, and ——, 2007: A simple, vertically resolved model of tropical disturbances with a humidity closure. *Tellus,* **59A,** 344–354.

Gill, A. E., 1980: Some simple solutions for heat-induced tropical circulation. *Quart. J. Roy. Meteor. Soc.,* **106,** 447–462.

Hsu P.-C., and T. Li, 2012: Role of the boundary layer moisture asymmetry in causing the eastward propagation of the Madden–Julian oscillation. *J. Climate,* **25,** 4914–4931.

Kim, D., and Coauthors, 2009: Application of MJO simulation diagnostics to climate models. *J. Climate,* **22,** 6413–6436.

Kiranmayi, L., and E. D. Maloney, 2011: Intraseasonal moist static energy budget in reanalysis data. *J. Geophys. Res.,* **116,** D21117, doi:10.1029/2011JD016031.

Kug, J.-S., K.-P. Sooraj, D. Kim, F.-F. Jin, I.-S. Kang, Y. Takayabu, and M. Kimoto, 2009: Simulation of state-dependent high-frequency atmospheric noise associated with ENSO in climate models. *Climate Dyn.,* **32,** 635–648, doi:10.1007/s00382-008-0434-2.

Lau, K. M., and L. Peng, 1987: Origin of low-frequency (intraseasonal) oscillations in the tropical atmosphere. Part I: Basic theory. *J. Atmos. Sci.,* **44,** 950–972.

Liebmann, B., and C. A. Smith, 1996: Description of a complete (interpolated) outgoing longwave radiation dataset. *Bull. Amer. Meteor. Soc.,* **77,** 1275–1277.

Lin, J.-L., and Coauthors, 2006: Tropical intraseasonal variability in 14 IPCC AR4 climate models. Part I: Convective signals. *J. Climate,* **19,** 2665–2690.

Madden, R. A., and P. R. Julian, 1972: Description of global-scale circulation cells in the tropics with a 40–50 day period. *J. Atmos. Sci.,* **29,** 1109–1123.

Majda, A. J., and S. N. Stechmann, 2009: The skeleton of tropical intraseasonal oscillations. *Proc. Natl. Acad. Sci. USA,* **106,** 8417–8422.

Maloney, E. D., 2009: The moist static energy budget of a composite tropical intraseasonal oscillation in a climate model. *J. Climate,* **22,** 711–729.

——, and D. L. Hartmann, 2000: Modulation of hurricane activity in the Gulf of Mexico by the Madden–Julian oscillation. *Science,* **287,** 2002–2004.

Mapes, B. E., and J. T. Bacmeister, 2012: Diagnosis of tropical biases and the MJO from patterns in the MERRA analysis tendency fields. *J. Climate,* **25,** 6202–6214.

Matsuno, T., 1966: Quasi-geostrophic motions in the equatorial area. *J. Meteor. Soc. Japan,* **44,** 25–43.

Matthews, A. J., 2008: Primary and successive events in the Madden–Julian oscillation. *Quart. J. Roy. Meteor. Soc.,* **134,** 439–453.

McBride, J. L., and R. Zehr, 1981: Observational analysis of tropical cyclone formation. Part II: Comparison of non-developing versus developing systems. *J. Atmos. Sci.,* **38,** 1132–1151.

Neelin, J. D., and J. Yu, 1994: Modes of tropical variability under convective adjustment and the Madden–Julian oscillation. Part I: Analytical theory. *J. Atmos. Sci.,* **51,** 1876–1894.

——, I. M. Held, and K. H. Cook, 1987: Evaporation–wind feedback and low-frequency variability in the tropical atmosphere. *J. Atmos. Sci.,* **44,** 2341–2348.

Raymond, D. J., 2000: Thermodynamic control of tropical rainfall. *Quart. J. Roy. Meteor. Soc.,* **126,** 889–898.

——, 2001: A new model of the Madden–Julian oscillation. *J. Atmos. Sci.,* **58,** 2807–2819.

Roundy, P. E., 2012: Observed structure of convectively coupled waves as a function of equivalent depth: Kelvin waves and the Madden–Julian oscillation. *J. Atmos. Sci.,* **69,** 2097–2106.

Sobel, A. H., and H. Gildor, 2003: A simple time-dependent model of SST hot spots. *J. Climate,* **16,** 3978–3992.

——, and E. D. Maloney, 2012: An idealized semi-empirical framework for modeling the Madden–Julian oscillation. *J. Atmos. Sci.,* **69,** 1691–1705.

——, and ——, 2013: Moisture modes and the eastward propagation of the MJO. *J. Atmos. Sci.,* **70,** 187–192.

——, J. Nilsson, and L. M. Polvani, 2001: The weak temperature gradient approximation and balanced tropical moisture waves. *J. Atmos. Sci.,* **58,** 3650–3665.

Sugiyama, M., 2009a: The moisture mode in the quasi-equilibrium tropical circulation model. Part I: Analysis based on the weak temperature gradient approximation. *J. Atmos. Sci.,* **66,** 1507–1523.

——, 2009b: The moisture mode in the quasi-equilibrium tropical circulation model. Part II: Nonlinear behavior on an equatorial β plane. *J. Atmos. Sci.,* **66,** 1525–1542.

Sukhatme, J., 2013: Low-frequency modes in an equatorial shallow water model with moisture gradients. *Quart. J. Roy. Meteor. Soc.,* in press.

Takayabu, Y. N., T. Iguchi, M. Kachi, A. Shibata, and H. Kanzawa, 1999: Abrupt termination of the 1997–98 El Niño in response to a Madden–Julian oscillation. *Nature,* **402,** 279–282.

Waliser, D. E., 2005: Predictability and forecasting. *Intraseasonal Variability of the Atmosphere–Ocean Climate System,* W. K. M. Lau and D. E. Waliser, Eds., Springer, 389–474.

Wang, B., 1988: Dynamics of tropical low-frequency waves: An analysis of the moist Kelvin wave. *J. Atmos. Sci.,* **45,** 2051–2065.

——, 2005: Theories. *Intraseasonal Variability of the Atmosphere–Ocean Climate System.* Springer, 307–360.

——, and H. Rui, 1990: Dynamics of the coupled moist Kelvin–Rossby wave on an equatorial plane. *J. Atmos. Sci.,* **47,** 397–413.

Wheeler, M. C., and G. N. Kiladis, 1999: Convectively coupled equatorial waves: Analysis of clouds and temperature in the wavenumber–frequency domain. *J. Atmos. Sci.,* **56,** 374–399.

——, and H. H. Hendon, 2004: An all-season real-time multivariate MJO index: Development of an index for monitoring and prediction. *Mon. Wea. Rev.,* **132,** 1917–1932.

——, and J. L. McBride, 2005: Australian-Indonesian monsoon. *Intraseasonal Variability in the Atmosphere–Ocean Climate System,* W. K. M. Lau and D. E. Waliser, Eds., Springer, 125–173.

Zhang, C., 2005: Madden-Julian oscillation. *Rev. Geophys.,* **43,** RG2003, doi:10.1029/2004RG000158.